The reduction of aqueous Au^{3+} by sulfide minerals and green rust phases

D.M. HEASMAN,[1,*] D.M. SHERMAN,[1] AND K.V. RAGNARSDOTTIR[1]

[1]Department of Earth Sciences, University of Bristol, Bristol, BS8 1RJ, U.K.

ABSTRACT

The reactions of Au^{3+} with green rust, stibnite, pyrite, and chalcopyrite were investigated in the laboratory and the size of the gold clusters formed was measured using extended X-ray absorption fine structure (EXAFS) spectroscopy, scanning electron microscopy (SEM), and transmission electron microscopy (TEM). The individual clusters produced were between approximately 29 Å and 77 Å in diameter and may occur individually or as composite clusters from hundreds to thousands of angstroms in size. This work shows that it is possible to form "invisible" gold through reduction of Au^{3+} by green rust phases and the surfaces of sulfide minerals.

INTRODUCTION

Understanding the mechanisms responsible for the accumulation of gold is essential for interpreting the history and genesis of known gold deposits. This information can then be used to prospect for new reserves. Within gold ores, gold is often found as submicroscopic grains associated with mineral surfaces and as inclusions within other minerals and this form is known as "invisible" gold. It is thought that "invisible" gold is formed by reduction of aqueous Au^+ or Au^{3+} by sulfide minerals and Fe^{2+} phases.

"Invisible" gold can be found in both primary and secondary gold deposits. In primary deposits, formed by hydrothermal activity, the "invisible" gold is usually associated with sulfide minerals (Foster 1984 and references therein). In secondary deposits, principally those formed by supergene enrichment in lateritic environments, "invisible" gold is primarily associated with iron (oxy)hydroxides (e.g., Darke et al. 1997).

The origin and nature of this type of gold is of particular interest because the form and distribution of gold within the ore affects the design and efficiency of the extraction process (Cook and Chryssoulis 1990; Hong et al. 1999). Cyanidation is the principal process by which gold is leached from oxygenated slurries of crushed ore (Fleming 1992) and "invisible" gold is not as amenable to cyanidation as other forms of gold found in ores (Spry and Thieben 2000). The effect of the presence of "invisible" gold on ore processing efficiency is demonstrated at the Hillgrove gold-antimony deposit (Australia) where it is estimated that up to 20% of the available gold is lost to tailings due to being present in this "invisible" form (Ashley et al. 2000).

The concentration and aqueous speciation of gold in natural solutions

The concentration of gold in natural solutions is typically 10^{-12} to 10^{-9} *M* (McHugh 1988; Vlassopoulos and Wood 1990a). The aqueous speciation of gold depends on the physico-chemical properties of the fluid.

Aqueous speciation in primary ore forming fluids. In hydrothermal systems the two ligands that are sufficiently abundant to complex gold, increasing its solubility and allowing

transport and subsequent concentration, are sulfide and chloride (Shenberger and Barnes 1989). Generally, in systems where the aqueous chloride concentration is low, the solutions are reducing and are up to temperatures of approximately 350 °C, sulfide is considered to be the most important ligand responsible for gold transport (Benning and Seward 1996 and references therein). In systems where sulfide concentration is low compared to chloride, and the solutions responsible for transport are acidic and oxidizing (Murphy et al. 2000) and the temperature is greater than 350 °C (Henley 1973), chloride is considered to be the most important ligand in transporting gold. Sulfide is chiefly responsible for gold transport in systems where the fluids are magmatic in origin (e.g., Matel et al. 2000) and chloride complexes are responsible for gold transport in systems where the fluids are meteoric (e.g., Mernagh et al. 1994) or oceanic in origin (e.g., Muller et al. 2001).

Experimental studies of gold solubility in high temperature sulfide solutions have shown that gold concentrations can reach between 10^{-5} and 10^{-4} *M* and that the gold is primarily transported as $AuHS^0$ and $Au(HS)_2^-$ (Seward 1973; Shenberger and Barnes 1989; Benning and Seward 1996).

Henley (1973) showed that high-temperature ($\leq$500 °C) chloride solutions can contain between 10^{-3} and 10^{-2} *M* gold and a Raman spectroscopy study of gold chloride solutions showed that up to 300 °C the gold forms complexes with the general formula $Au^{3+}Cl_xOH_{(4-x)}^-$, with the value of *x* dependant on pH (Murphy et al. 2000). It is likely that in chloride-dominated systems that some reduction of gold will occur and therefore some of the gold will be present as Au^+. The use of Au^{3+} in the work presented here is justified because firstly, some gold in these systems will be present as Au^{3+} and secondly, since the reduction of Au^{3+} by mineral surfaces is a two stage process (Mycroft et al. 1995; Eqs. 1 to 5 below) Au^{3+} represents a convenient and stable precursor for Au^+ (Maddox et al. 1994).

Aqueous speciation in secondary ore forming fluids. The solubility, and therefore the transport, of gold in oxidizing secondary ore forming environments has traditionally been attributed to chloride (Krauskopf 1951; Cloke and Kelly 1964) but more recent work on the dissolution of metallic gold in sodium hydroxide solutions by Vlassopoulos and Wood (1990a, 1990b) suggests that the Au^+ species $AuOH(H_2O)^0$ is the dominant aque-

* E-mail: heasman@geol.uniovi.es

ous species in most circum-neutral, oxidized natural waters (Fig. 1). However, spectroscopic studies on the aqueous complexation of gold have failed to identify the AuOH(H$_2$O)^0 complex in solution. Raman and UV/Vis. (Peck et al. 1991), Raman (Murphy and Lagrange 1998), extended X-ray absorption fine structure (EXAFS), and X-ray absorption near edge spectroscopic (XANES) (Farges et al. 1993) studies have observed the Au^{3+} species AuCl$_4^-$ at low pH values and as the pH was increased the chloride ligands were successively replaced by OH ligands with none or minor Au$^+$ species observed. These observations are in direct contradiction with the speciation predicted using the ΔG_{f298}^0 of AuOH(H$_2$O)^0 calculated by Vlassopoulos and Wood (1990a, 1990b) (Fig. 1; plotted using the experimental composition of Murphy and Lagrange 1998). This contradiction suggests that the oxidation of aqueous gold may be kinetically controlled and if the dissolution experiments of Vlassopoulos and Wood (1990a, 1990b) had been left for a longer period of time then Au^{3+} would have been observed in the experimental solutions. All of the spectroscopic studies of aqueous gold speciation used Au^{3+} salts to produce their experimental solutions; therefore any potential kinetic effects on the oxidation state of gold would not have affected the results. In the EXAFS study of aqueous gold speciation by Farges et al. (1993) the same Au^{3+} solutions were analyzed again after 5 months and there was no distinguishable difference in the EXAFS data produced. In addition to the contradiction between the results of the dissolution experiments and the spectroscopic observations this suggests that the oxidation rate of aqueous Au$^+$ to aqueous Au^{3+} has been underestimated and that once the oxidation is complete the Au^{3+} produced is stable. Therefore, aqueous gold may be present in oxidized natural solutions as Au^{3+}.
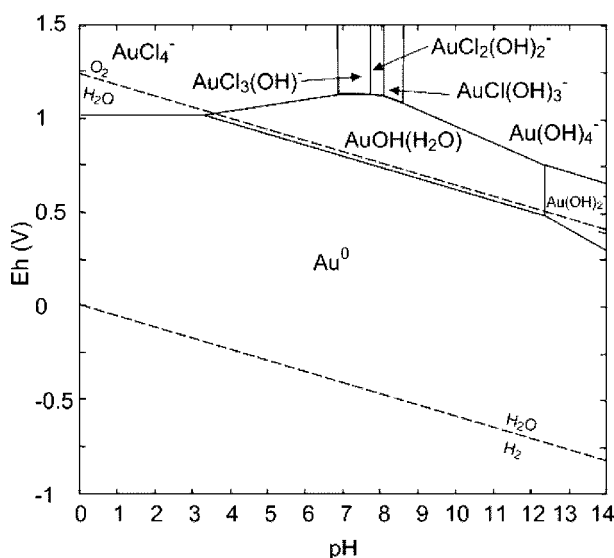

FIGURE 1. Eh/pH diagram for the system Au-Cl-H$_2$O. Composition is the same as Murphy and LaGrange (1998) used in their Raman experiments (0.02 M HAuCl$_4$·4H$_2$O) and the ΔG_{f298}^0 of AuOH(H$_2$O)^0 is from Vlassopoulos and Wood (1990b). The diagram is calculated from the thermodynamic data presented in Table 1 using Geochemists Workbench (Bethke 1994).

"Invisible" gold associated with sulfide minerals

Adsorption and/or reduction of gold in solution by mineral surfaces to form metallic gold have only recently been invoked as a mechanism for gold accumulation in hydrothermal systems. Observations from the active hydrothermal system at Broadlands, New Zealand have shown that economic concentrations of gold (associated with arsenic and antimony sulfides) can form from fluids containing gold concentrations almost as low as seawater (0.04 µg/kg) (Seward 1984). Experimental work on the adsorption of aqueous gold to amorphous antimony and arsenic sulfides has shown that the concentration of gold found in the Broadlands system could have accumulated due to the adsorption of aqueous gold alone (Renders and Seward 1989). ^{197}Au Mössbauer spectroscopy of these experimental systems confirms that gold is present as complexes at the surface of amorphous antimony and arsenic sulfides and not as metallic gold (Cardille et al. 1993). However, metallic gold is also found in association with stibnite in ancient hydrothermal systems that are now being mined (e.g., Michibayashi 1995; Berzon et al. 1999; Mehrabi et al. 1999). Further work is needed to decide whether this metallic gold is reduced by longer-term processes involving the mineral surface or by some external reducing agent. Adsorption alone could produce interlattice "invisible" gold because adsorbed gold could be incorporated into the lattice of the adsorbent by subsequent precipitation of new mineral layers. To form the angstroms to micron-sized metallic gold grains observed in some natural samples (e.g., Mehrabi et al. 1999), however, reduction would be required.

The commonest sulfide phase with which "invisible" gold is associated is pyrite (e.g., Mao 1991; Santaguida and Hannington 1996; Yang et al. 1998) and it is this mineral that has attracted the most experimental attention with respect to gold adsorption and reduction. Jean and Bancroft (1985) found that Au^{3+} is rapidly adsorbed from solution and then reduced to Au^0 at the surface of pyrite via an Au$^+$ intermediate phase. This reaction is accompanied by oxidation of the pyrite to aqueous Fe^{3+} and sulfate or the formation of polysulfides and elemental sulfur on the pyrite surface (Hyland and Bancroft 1989). The

TABLE 1. Summary of thermodynamic data used to plot the Eh-pH diagram in Figure 1

Species	ΔG_{f298} (KJ/mol)	Species	ΔG_{f298} (KJ/mol)
H$_2$O	−237.2*	AuOH^{2+}	185.057†
OH$^-$	−157.3*	Au(OH)$_2^+$	−63.639†
Cl$^-$	−131.3*	Au(OH)$_4^-$	−455§
Au^0(aq)	53.591†	Au(OH)$_3$Cl$^-$	−404§
Au$^+$	163.6‡	Au(OH)$_2$Cl$_2^-$	−350§
Au^{3+}	440§	Au(OH)Cl$_3^-$	−294§
AuOH(H$_2$O)^0	−345.6#	AuCl$_2$OH(H$_2$O)^0	−386§
AuOH^0	−61.964†	AuH$_2$OCl$_3^0$	−311§
Au(OH)$_2^-$	−276.32†	AuCl^{2+}	239.485†
Au(OH)Cl−	−219.388†	AuCl$_2^+$	70.757†
AuCl$_2^-$	5.024†	AuCl$_3^0$	−83.317†
AuCl$_2^-$	−151.143^2	AuCl$_4^-$	−234.6§

* Stumm and Morgan (1981).
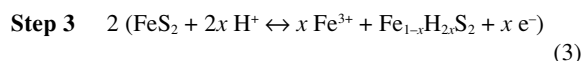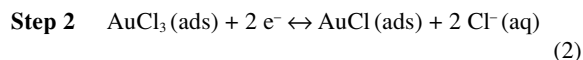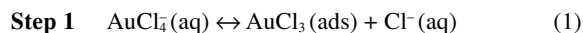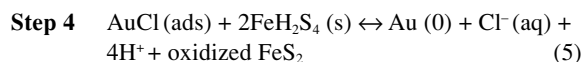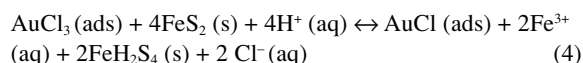† Baranova and Rhyzenko (1981).
‡ Renders and Seward (1989).
§ Baes and Mesmer (1976).
# Vlassopoulos and Wood (1990b).

rate of gold deposition is controlled almost entirely by the rate of reduction of Au^{3+} and the particles of Au^0 formed on the pyrite surface consist of composite particles approximately 3800 Å in diameter (Maddox et al. 1994). A study of the kinetics of this system (Mycroft et al. 1995) has confirmed the existence of these steps, which are summarized below:

Step 1 $\quad AuCl_4^- (aq) \leftrightarrow AuCl_3 (ads) + Cl^- (aq)$ (1)

Step 2 $\quad AuCl_3 (ads) + 2\,e^- \leftrightarrow AuCl (ads) + 2\,Cl^- (aq)$ (2)

Step 3 $\quad 2\,(FeS_2 + 2x\,H^+ \leftrightarrow x\,Fe^{3+} + Fe_{1-x}H_{2x}S_2 + x\,e^-)$ (3)

Steps 2 and 3 combined ($x = 1$)

$AuCl_3 (ads) + 4FeS_2 (s) + 4H^+ (aq) \leftrightarrow AuCl (ads) + 2Fe^{3+}$ (aq) $+ 2FeH_2S_4 (s) + 2\,Cl^- (aq)$ (4)

Step 4 $\quad AuCl (ads) + 2FeH_2S_4 (s) \leftrightarrow Au (0) + Cl^- (aq) +$ $4H^+ +$ oxidized FeS_2 (5)

The electrons for the reduction are supplied by step 3, which removes the Fe^{2+} from the pyrite lattice where it is oxidized. SEM imaging of the reacted pyrites revealed that the metallic gold clusters formed were of approximately equal size (500–1000 Å), "suggesting an instantaneous nucleation and growth mechanism" (Mycroft et al. 1995).

"Invisible" gold is also found associated with chalcopyrite (e.g., Hannington et al. 1991; Bowell et al. 1999), sphalerite (e.g., Rubin and Kyle 1997), arsenopyrite (e.g., Fleet and Mumin 1997), pyrrhotite (e.g., Oberthur et al. 1997), and marcasite (e.g., Fleet and Mumin 1997). Jean and Bancroft (1985) included chalcopyrite, sphalerite, and pyrrhotite in their study and showed that, like pyrite, these sulfide mineral surfaces can rapidly adsorb aqueous gold and reduce it to metallic gold.

"Invisible" gold associated with iron oxy(hydroxides)

The "invisible" gold in supergene laterite deposits is thought to form by two processes, either acting individually or in combination with each other: adsorption to iron minerals and ferrolysis (Eq. 6). Adsorption studies have focused on the two main iron minerals found in lateritic deposits, hematite, and goethite (Valeton 1994 and references therein). Gold adsorbs to both minerals and whilst hematite is considered to be an effective scavenger of gold as aqueous complexes (Nechayev 1984; Karasyova et al. 1998) and as colloids (Enzweiler and Joekes 1991), goethite does not accumulate gold to ore grades (Machesky et al. 1991; Schoonen et al. 1992). Whether the mineral is an effective scavenger of gold or not, adsorption could be responsible for the formation of inter-lattice "invisible" gold since any gold adsorbed to either of these minerals could be incorporated into the mineral lattice as new layers of iron (oxy)hydroxide are precipitated on pre-existing mineral grains. Ferrolysis refers to the reduction of aqueous Au^{3+} by aqueous Fe^{2+} from the bedrock (Mann 1984) and can be sum-

marized by the following reaction:

$$AuCl_4^- + 3\,Fe^{2+} + 6\,H_2O \leftrightarrow Au^0 (s) + 3\,FeOOH (s) + 9\,H^+$$ (6)
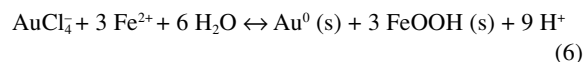
However, this relatively straightforward mechanism may be more complex due to the formation of intermediate iron oxy(hydroxide) phases such as green rusts. Green rusts, $[Fe_4^{2+}Fe_2^{3+}(OH)_{12}X_y$, where X is typically Cl^- ($y = 2$) or SO_4^{2-} ($y = 1$)], were first identified as the products of the corrosion of steel in earth surface environments (Schwertmann and Fetcher 1994) and due to the sensitivity to oxidation they have only recently been identified in natural systems, such as ochre sludges in Denmark (Bender Koch and Mörup 1991). Green rusts contain a mixture of Fe^{3+} and Fe^{2+} and thus only partial oxidation of the aqueous Fe^{2+} is required for them to form. On further exposure to an oxidizing agent they fully oxidize to goethite or lepidocrocite. It is likely that in oxidizing groundwater where complexes of aqueous Au^{3+} are stable any aqueous Fe^{2+} present will at least be partially oxidized because the standard potential for the Fe^{2+} to Fe^{3+} half reaction is higher than the standard potential for the half reaction Au^0 to Au^{3+} (–0.77 V and –1.4 V, respectively; Atkins 1994). Thus the $AuCl_4^-$ (aq) species in Equation 6 can probably be reduced by an intermediary solid phase such as green rust and not solely by aqueous Fe^{2+}.

The aim of this study is to react aqueous Au^{3+} with minerals that could act as reductants. Then, using EXAFS spectroscopy, SEM, and TEM, to determine if metallic gold particles are formed and to constrain the size of the particles produced to determine if the gold is indeed "invisible."

MATERIALS AND METHODS

General

Reagents used in this study were of analytical grade or higher and were supplied by Fisher Scientific. All apparatus were acid washed and MilliQ (18.2 MΩ) water was used for all stages of the experiments. The pH measurements were made using "Wilhelm" style electrodes (Sentek U.K. Ltd.) connected to an Orion model 720A pH meter or to a Metrohm auto-titrator (Metrohm U.K. Ltd. Titrino model 718). Electrodes were calibrated using constantly stirred certified buffers (4.007 ± 0.012, 6.869 ± 0.012, and 9.180 ± 0.012, Schott Gerate) stored in a water bath to ensure temperature equivalence with the experiments. Calibrations were only accepted if the R^2 value of the calibration curve was better than 98%. Light was excluded from all preparations to avoid any possible photochemical reactions.

In all cases the samples were centrifuged for 20 min at 3300 rpm following which the supernatant was removed and filtered using a 0.2 mm nitrocellulose filter mounted in a polypropylene filter housing. The filtrate was then quantitatively diluted by 10 using 1% v/v HCl (aq) and these solutions were analyzed for dissolved species of interest by inductively coupled plasma atomic-emission spectroscopy (ICP-AES). A Jobin Yvon JY 24 ICP-AES was calibrated using a series of standards produced by serial dilution of 1000 ppm stock solutions (Fisher Scientific, ICP grade). All calibrations had R^2 values better than 99% (typically 99.99%). Small amounts of the wet pastes pro-

duced were mounted in Teflon sample holders at room temperature using Sellotape. These were then frozen in liquid nitrogen and stored in a freezer for subsequent analysis using EXAFS and XANES spectroscopies.

The remaining wet pastes were analyzed using SEM and TEM in an attempt to measure the size of any gold particles present. X-ray diffraction (XRD) was used to identify the solid phases present. The wet pastes were mixed with a small amount of glycerol to prevent oxidation during analysis and were mounted on glass slides to be analyzed using Cu$K\alpha$ radiation on a Philips PW 1800 X-ray powder diffractometer.

Green rust sample preparation

Green rust was prepared using the method of Schwertmann and Fetcher (1994). All samples were taken via self-sealing rubber septa using a 20 mL polypropylene syringe with a 50 mm stainless steel needle attached. Samples were immediately transferred to 50 mL polypropylene centrifuge tubes purged with argon gas and then sealed with Teflon® tape. Sample preparation took place in a 500 mL polypropylene gas tight reaction vessel in a water bath maintained at 25 °C (±0.01 C) by a Haake DC5 heater/circulator and a cooling circuit connected to a tap water supply. Initially the vessel contained 300 mL of water purged with nitrogen gas for 12 hours. The purge gas was then changed to argon gas prior to addition of a known weight of $FeSO_4 \cdot 7H_2O$ (s) (approximately 20 g). The pH was then raised from an initial value of ~3.4 to 7.0 over 15 min by the addition of carbon dioxide free 1 M sodium hydroxide by a Metrohm 718 pH-Stat titrator. Once pH 7 was reached the argon gas supply was replaced by a laboratory air supply provided by a small pump. Initial experiments had shown that three hours of oxidation were required for a complete transformation of the aqueous Fe^{2+} to green rust. At the end of the initial oxidation step a 20 mL sample of the suspension was removed for analysis by XRD, to confirm that the dark blue green precipitate formed was green rust, and a filtered sample was analyzed by ICP-AES, to measure aqueous iron enabling quantification of the amount of green rust produced. Immediately a known volume of a 5543 ppm stock solution of $HAuCl_4$ was added to give final gold concentrations of 0.1 wt% [(weight of gold/theoretical yield of green rust) × 100]. The initial experiments had shown that 100% of the aqueous gold was removed from solution within 10 min of gold addition. At this point two samples were taken; one was frozen and used for EXAFS analysis and the other was separated as above and was analyzed by XRD and ICP-AES. The preparation was repeated to produce a sample with 0.5 wt% gold.

Sulfide sample preparation

All sulfide minerals (stibnite, pyrite, and chalcopyrite) used in this study were obtained as powders from the Earth Sciences collection at the University of Bristol and were of unknown origin. A few grams of each mineral were washed using 1% v/v hydrochloric acid to remove any oxidized species from the surface and dried at room temperature under argon gas. Approximately 5 g of each mineral was then transferred to a 50 mL, argon gas purged, polypropylene centrifuge tube and 10 mL of each of the following solutions was added; 3 M NaCl, 18.2 MΩ water, and 5036 ppm $HAuCl_4$. The tubes were then

sealed using Teflon tape and were shaken in a Grant SS30 water bath maintained at 25 °C (±1 °C) for 12 hours. At the end of this time the samples were separated as before so that the supernatant could be analyzed by ICP-AES for aqueous gold and the wet pastes produced were analyzed using EXAFS, XANES, SEM, and TEM. Analysis of the supernatant for copper, antimony, and iron using ICP-AES showed that all of these cations were present in the supernatants below detection limits of the ICP-AES (9.7, 8.4, and 10 ppb, respectively) and therefore there was no detectable mineral dissolution over the duration of the experiments.

EXAFS sample preparation and analysis

The slides were transported to a synchrotron laboratory in a plastic bottle floating in liquid nitrogen and were placed in a freezer upon arrival. In addition to the green rust and sulfide samples spectra were also collected from a 10 μm thick gold foil. EXAFS data were collected at the Central Laboratory of the Research Councils Synchrotron Radiation Source at Daresbury, U.K. Samples were mounted on a liquid nitrogen cryostat. EXAFS and X-ray absorption near edge spectroscopy (XANES) spectra were collected in fluorescence mode at the Au L-III edge (11919 eV) on station 9.3, which is equipped with a harmonic-rejecting double crystal Si (220) monochromator. Each sample was scanned for 45 min 8 to 18 times. The storage ring energy was 2 GeV and the beam current varied between 100 and 240 mA.

EXAFS data reduction was performed using Daresbury Laboratory software packages (EXCALIB, modified to allow for the non-linearity of the detector at high count rates, and EXBACK; Dent and Mosselmans 1992). EXCALIB was used to calculate energy (eV) from the monochromator position (in millidegrees) to and to average multiple spectra from individual samples. EXBACK was used to define the start of the EXAFS oscillations (determined from the inflection point on the L-III edge) and perform background subtraction. The pre-edge was fitted to a linear function and the post-edge background to two second-order polynomial segments. The EXAFS oscillations were simulated using the exact curved wave theory (Gurman et al. 1984; Gurman 1988) as implemented in the EXAFS analysis program EXCURV98 (Binstead et al. 1998). The phase-shift functions used in the curve fitting process were derived by ab initio methods in EXCURV98 using Hedin-Lundqvist potentials (Hedin and Lundqvist 1969) and von Barth ground states. No Fourier filtering was performed during the data analysis and all the shells were fitted without constraint.

Initially a value for the R-factor (the fitting parameter) for the first co-ordination shell in each sample was generated by optimizing co-ordination number (N), shell radius (R) and Debye-Waller factor (DWF) for each element present in the system. The element that gave the best fit (i.e., the lowest value of the R-factor) was then assigned to that shell. This was repeated for successive shells and only shells that decrease the R-factor by 5% were included in the final fit.

Scanning electron microscope (SEM) imaging and energy dispersive X-ray (EDX) scanning

To confirm that the samples contain submicroscopic particles of gold, as deduced from the EXAFS and XANES analy-

sis, SEM images of all of the samples were collected using a Hitachi S/2300 scanning electron microscope fitted with an EDX detector. Aliquots of the samples analyzed by EXAFS and XANES spectroscopies were dried overnight at room temperature under argon gas, and subsequently were mounted directly onto carbon pads in a glove box under nitrogen gas, then were coated with carbon and loaded directly into the SEM. During the coating and loading stage it was not possible to exclude oxygen. Initially low magnification images were scanned with the EDX detector to locate gold within the sample. Based on these data small areas where gold was known to be present were selected for collection of a higher magnification image.

Transmission electron microscope (TEM) imaging and EDX analysis

To further constrain the size of the gold particles produced in these experiments the samples were also imaged using a JEOL JSM 5600LV transmission electron microscope. Separate aliquots of the wet pastes analyzed using EXAFS and XANES spectroscopies were suspended in 18.2 MΩ water, were placed on a copper grid using a transfer pipette and then loaded into the TEM. All stages of the sample preparation for TEM analysis were performed without exclusion of oxygen. To ensure that the images obtained represented areas of the sample where gold is present, an EDX detector was used to qualitatively measure the chemical composition of the area of the sample represented by the image.

Calculation of gold cluster sizes and co-ordination environment

Benfield (1992) presented formulae that relate the co-ordination number in the first shell (N_1) in metallic clusters to the size of the cluster (valid for values of $N_1 < 12$). The formulae allow N_1 to be calculated for a cluster of edge length m (atoms). For a cuboctahedron:

$$N_1(\text{cuboct}) = 12 \frac{(m-1)(10m^2 - 14m + 6)}{(2m-1)(5m^2 - 5m + 3)} \quad (7)$$

The number of atoms in the cluster (N_t) can also be calculated:

$$N_t = \frac{(2m-1)(5m^2 - 5m + 3)}{3} \quad (8)$$

Once m has been calculated it can be multiplied by the atomic diameter of gold (Å) to give the edge length of the cluster, and since the radius of a sphere circumscribing a cuboctahedron equals the edge length, the cluster diameter can be easily calculated.

Calculation of m also allows predictions of the co-ordination number for the subsequent four shells to be made for comparison with EXAFS results. The average co-ordination numbers for each of the shells were calculated using the formulae for the populations of the different sites (interstitial, vertex, edge, square face, and triangular face) present within a cuboctahedral cluster presented by Benfield (1992) (Table 2). The co-ordination of each site for the first five shells was then measured using the structure for face centered cubic (FCC) bulk gold

from Fletcher et al. (1996) (Table 2).These two calculations were then used in conjunction with the formula for N_t (Eq. 8) to produce expressions for the average N_x ($2 < x < 5$) for each shell as a function of edge length (m) (Table 3).

RESULTS AND DISCUSSION

Characterization of green rust and sulfide minerals

Comparison of the reference XRD diffractograms with the experimental data shows that all of the samples contain no other detectable minerals except that the chalcopyrite sample appears to contain a minor amount of chalcocite (CuS). The BET surface areas of the stibnite, pyrite, and chalcopyrite samples were measured as 3.33, 3.3, and 6.59 m²/g, respectively.

Qualitative analysis of XANES spectra

The XANES regions of the EXAFS spectra collected for each sample are shown in Figure 2. Figure 2 also shows spectra of reference compounds containing the two principal oxidation states of aqueous gold found in nature: Au^{3+} ($KAuCl_4$; Farges et al. 1993) and Au^+ (sodium gold thiomalate, AuSTm; Watkins et al. 1987). The reference spectrum for metallic gold was obtained from a 10 μm thick gold foil. Comparison of the reference spectrum to the experimental data clearly shows that gold is present as metallic gold in all of the samples analyzed. All experimental spectra show the same two absorption maxima as the gold foil spectrum (feature **a**, Fig. 2); none of the experimental spectra contain the absorption maxima characteristic of Au^{3+} (feature **b**, Fig. 2) present in the $KAuCl_4$ spectra and none of the experimental spectra resemble the relatively featureless

TABLE 2. Population and co-ordination of the different sites in a cuboctahedral cluster in terms of edge length m (atoms)

Site	Population	Co-ordinations				
		N_1	N_2	N_3	N_4	N_5
Interstitial	$\frac{(2m-3)(5m^2-15m+13)}{3}$	12	6	24	12	24
Vertex	12	5	2	6	5	5
Edge	$24(m-2)$	7	3	10	7	10
Square Face	$6(m-2)^2$	3	5	8	12	16
Triangular Face	$4(m-3)(m-2)$	9	3	13	5	12

TABLE 3. Expressions for the average co-ordination environment of each of the first five shells present in a cuboctahedral cluster

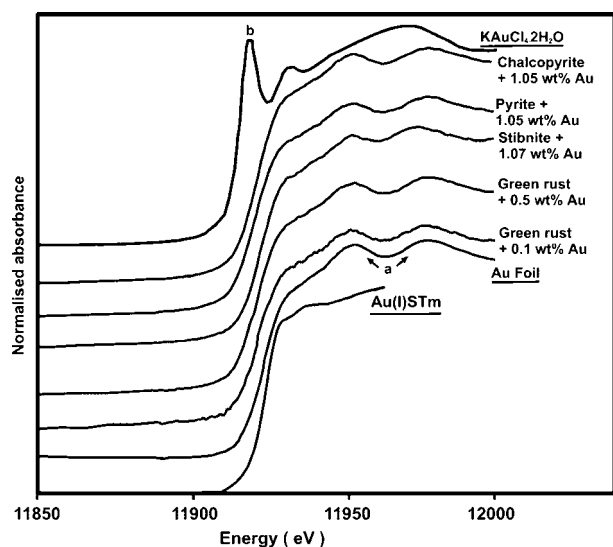| Shell	Average Co-ordination
N_2	$6\dfrac{10m^3 - 24m^2 + 17m - 3}{(2m-1)(5m^2-5m+3)}$
N_3	$12\dfrac{20m^3 - 59m^2 + 65m - 30}{(2m-1)(5m^2-5m+3)}$
N_4	$24\dfrac{5m^3 - 14m^2 + 20m - 15}{(2m-1)(5m^2-5m+3)}$
N_5	$24\dfrac{5m^2 + 11m + 6}{5m^2 - 5m + 3}$

FIGURE 2. XANES spectra of all of the samples analyzed by EXAFS. Also included are reference XANES spectra for the three principal oxidation states of gold (underlined).

spectra of AuSTm. The XANES spectra also contain some information about the size of the metallic gold clusters. Generally the intensity and width of the absorption maxima (feature **a**, Fig. 2) present in the spectra for metallic gold clusters are directly related to the number of neighbors and, more generally, to the size of the gold clusters (Benfield et al. 2001). Figure 2 shows that the sizes of these two maxima in the normalized spectra of the samples are similar to that of gold foil. This suggests the presence of at least five to six shells of gold atoms (Benfield et al. 2001) and that the clusters are at least 36 to 43 Å in diameter.

EXAFS spectra of gold foil

The k^3 weighted EXAFS spectrum of gold foil is shown in Figure 3a and the Fourier transforms of these data and the interpretation of the co-ordination environment in this foil is shown in Figure 3b. In these figures and all subsequent figures containing EXAFS data the thin line represents the experimental data and the bold line represents the calculated theoretical spectrum. The Debye Waller factors are also given (DWF). Calculation of the theoretical co-ordination environment within bulk gold shows that it contains 12 atoms at 2.88 Å, 6 atoms at 4.08 Å, 24 atoms at 4.99 Å, 12 atoms at 5.77 Å, and 24 atoms at 6.45 Å (Fletcher et al. 1996), which is in very good agreement with the distances observed in the EXAFS data presented here (Fig. 3b).

EXAFS spectra of gold after reaction with green rust and sulfide minerals

The k^3 weighted spectra for gold after reaction of aqueous Au³⁺ with green rust and after reaction with the sulfide minerals are shown in Figures 4a and 5a, respectively. The Fourier transforms of the k^3 weighted EXAFS spectra and the interpretations of the co-ordination environments in these samples are

shown in Figures 4b (green rust samples) and 5b (sulfide samples).

Metallic gold can form cuboctahedral and icosahedral clusters (Benfield 1992; Fritsche and Benfield 1993) and these two cluster types have different co-ordination numbers (N) at different distances R (Å) (Table 4).

Comparison of these two co-ordination environments with the EXAFS data for all samples shows that the metallic gold is crystallizing as cuboctahedral clusters because no indication of the third, fifth, and sixth shells (4.18, 5.16, and 5.24 Å, respectively) of the icosahedral geometry is observed in the EXAFS data. In all of the samples the distances predicted using a cuboctahedral geometry (using values of R_x/R_1 from Benfield 1992) are in very good agreement with the measured distances (Table 5). All measured distances agree with the predicted distances to within 1.5%.

The co-ordination numbers predicted by the cuboctahedral geometry agree with the measured values within the ±20% error in N associated with EXAFS results, except for the third shell in the green rust sample with 0.1 wt% gold, which differs

TABLE 4. Comparison of the co-ordination environments of cuboctahedral and icosahedral gold clusters

	Cuboctahedral			Icosahedral		
Shell	R	R_x/R_1	N	R	R_x/R_1	N
1	2.88	1	12	2.88	1	6
2	4.07	1.41	6	3.03	1.05	6
3	4.99	1.73	24	4.18	1.45	6
4	5.76	2.00	12	4.90	1.70	6
5	6.44	2.24	24	5.16	1.79	12
6	7.05	2.45	8	5.24	1.82	6
7	7.62	2.65	48	5.76	1.97	6
8	8.15	2.83	6	6.06	2.00	6
9	8.64	3.00	36	6.51	2.10	12
10	9.11	3.16	24	2.26	2.26	12

Note: R_x/R_1 equals the ratio of the distance of shell x to the distance of the first shell.

TABLE 5. Comparison of shell distances observed in the EXAFS data with those predicted for cuboctahedral gold clusters

Sample	Measured R_1	Predicted R_2	Measured R_2	Predicted R_3	Measured R_3
Gold Foil	2.87	4.06	4.06	4.97	5.00
Green rust + 0.1 wt% Au	2.86	4.04	4.05	4.95	4.98
Green rust + 0.5 wt% Au	2.87	4.06	4.06	4.97	5.00
stibnite + 1.07 wt% Au	2.88	4.08	4.07	4.99	5.00
pyrite + 1.05 wt% Au	2.87	4.06	4.07	4.97	4.98
chalcopyrite + 1.02 wt% Au	2.87	4.05	4.07	4.96	4.98

Sample	Measured R_1	Predicted R_4	Measured R_4	Predicted R_5	Measured R_5
Gold Foil	2.87	5.73	5.67	6.41	6.44
Green rust + 0.1 wt% Au	2.86	5.71	NP	6.38	NP
Green rust + 0.5 wt% Au	2.87	5.74	5.67	6.42	NP
stibnite + 1.07 wt% Au	2.88	5.77	5.68	6.45	6.42
pyrite + 1.05 wt% Au	2.87	5.74	5.67	6.41	6.42
chalcopyrite + 1.02 wt% Au	2.87	5.73	5.66	6.41	6.43

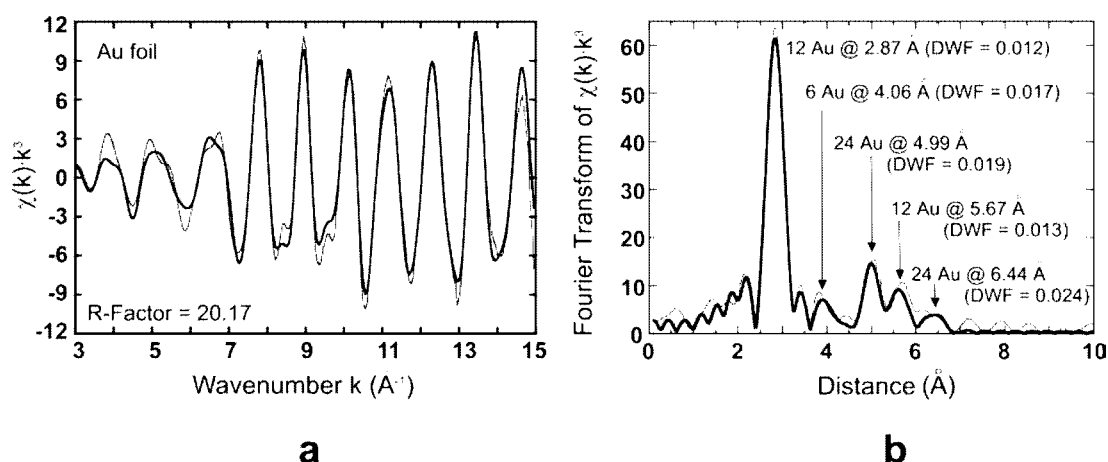*Note:* NP = shell not present.

FIGURE 3. (**a**) k^3 weighted EXAFS spectrum for gold foil. (**b**) Fourier transform of the k^3 weighted EXAFS spectrum shown in **a**.

TABLE 6. Comparison of co-ordination numbers observed in the EXAFS data with those predicted for cuboctahedral gold clusters

Sample	Measured N_1	Predicted N_2	Measured N_2	Predicted N_3	Measured N_3
Green rust + 0.1 wt% Au	11.67	5.84	5.80	22.97	14.50
Green rust + 0.5 wt% Au	9.46	4.64	4.40	16.65	18.45
stibnite + 1.07 wt% Au	9.13	4.45	3.98	15.77	18.45
pyrite + 1.05 wt% Au	10.94	5.45	5.32	20.74	18.29
chalcopyrite + 1.02 wt% Au	10.80	5.38	4.69	20.33	18.24

Sample	Measured N_1	Predicted N_4	Measured N_4	Predicted N_5	Measured N_5
Green rust + 0.1 wt% Au	11.67	11.55	NP	23.13	NP
Green rust + 0.5 wt% Au	9.46	9.17	8.81	17.27	NP
stibnite + 1.07 wt% Au	9.13	8.88	5.02	16.38	15.51
pyrite + 1.05 wt% Au	10.94	10.64	9.37	21.1	17.15
chalcopyrite + 1.02 wt% Au	10.80	10.48	10.83	20.80	20.56

Note: NP = shell not present.

by 37%, and the fourth shell in the stibnite sample, which differs by 43% (Table 6). It seems, therefore, that using the cuboctahedral geometry is a valid method to calculate the size of the gold clusters present in these samples.

Calculation of gold cluster size

The results of the cluster size calculations are shown in Table 7. Cluster sizes have also been calculated including the error of ±20% in N_1. The results show that for all of the samples, except for green rust with 0.5 wt% gold and stibnite, the clusters produced are at the upper size limit that is resolvable with this technique in these types of systems because the error in N_1 produces greater variations in diameter as N_1 approaches 12.

However, these data can be used to provide a lower size limit for the gold clusters produced in this experiment of ap-

proximately 20 to 250 Å. Further constraints can be put on these sizes because in all of these samples (except for the green rust samples) five shells, that have co-ordination numbers in good agreement (i.e., within ±20%) with the predicted values, are present. In cuboctahedral clusters the edge length (m) is equivalent to the number of co-ordination shells present in the cluster. Therefore these data suggest that the value of m in these samples is at least 5, which corresponds to a cluster diameter of 36 Å.

In the green rust sample with 0.1 wt% gold, only three shells are observed in the EXAFS data. We do not think, however, that this represents a cluster with a maximum value of $m = 3$ because the first shell contains 11.67 gold atoms, which corresponds to a cluster diameter of 241 Å, suggesting there are more than 3 shells present. It is more likely that the fourth and fifth shells are not shown in the EXAFS spectrum because the concentration of gold in this sample is low, resulting in poorer quality spectra (the R-factor is 42.32). However, the XANES spectrum of this sample qualitatively suggests that at least five shells are present and therefore the clusters are at least 36 Å in size (see above section "Qualitative Analysis of XANES spectra"). In the green rust sample with 0.5 wt% gold only four shells are detectable in the EXAFS data. A cluster with $m = 4$ would have a diameter of 28.64 Å, which is in good agreement with the measured size of the clusters in this sample. Given the good fit to the EXAFS data (R-factor of 25.65) it is thought that the clusters present in this sample contain between four and five co-ordination shells of gold atoms that represent an average cluster size of between 28.64 and 36 Å. Some qualitative evidence for the presence of this number of shells is also contained in the XANES spectrum of this sample (see above section "Qualitative Analysis of XANES spectra").

SEM and EDX analysis

Figures 6 to 10 depict the SEM images and EDX scans of the samples analyzed in this work. Figures 6a and 7a show the images of the green rust samples at low magnification (×3000) with the EDX data overlain and Figures 6b and 7b show the higher magnification (×10 000) images of the green rust samples and the EDX scans taken of these views. In these and subse-
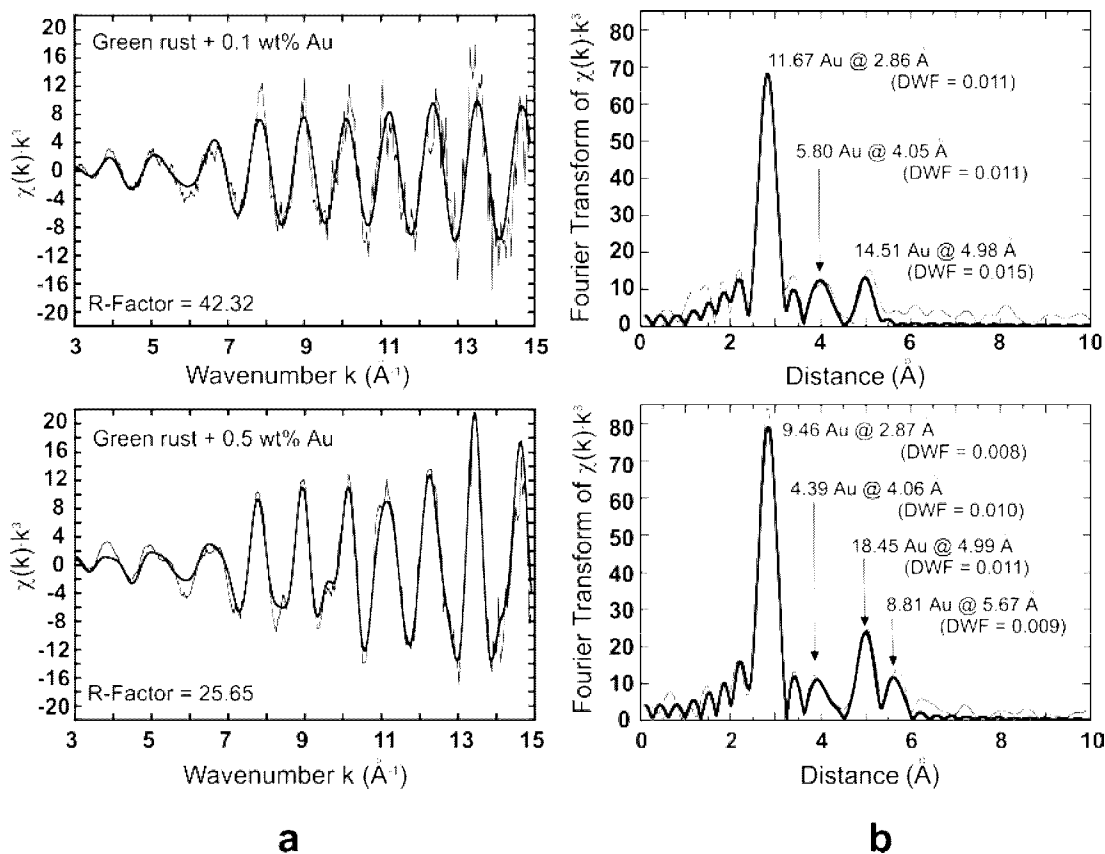
FIGURE 4. (**a**) k^3 weighted EXAFS spectra for gold after reaction of aqueous Au^{3+} with green rust. (**b**) Fourier transforms of the k^3 weighted EXAFS spectra.

TABLE 7. Results of cluster size calculations for all samples analyzed by EXAFS

Sample	N_1	Diameter Å	N_1 −20%	Diameter Å	N_1 +20%	Diameter Å
Green rust + 0.1 wt% Au	11.67	241	9.34	32	14.01	
Green rust + 0.5 wt% Au	9.46	34	7.57	20	11.36	123
Stibnite + 1.07 wt% Au	9.13	30	7.30	19	10.95	77
Pyrite + 1.05 wt% Au	10.94	76	8.75	27	13.13	
Chalcopyrite + 1.02 wt% Au	10.80	68	8.64	26	12.96	

Note: The blank fields represent results when $N_1 > 12$.

quent images the presence of gold is indicated by the black dots. Figures 8a, 9a, and 10a show the initial low magnification images of the sulfide samples and EDX scans. Figures 8b, 9b, and 10b present the higher magnification images of the gold-containing areas marked with a black rectangle in the lower magnification images.

The absence of any obvious features that can be identified as gold clusters in the high magnification images (Figs. 6b, 7b, 8b, 9b, and 10b) suggests that the metallic gold clusters seen in the EXAFS data are smaller than the minimum size resolvable on a SEM (0.5 μm, 5000 Å) and are indeed sub micrometer or "invisible" gold particles (Yang et al. 1998).

TEM and EDX analysis

Figure 11 shows the TEM images and EDX spectra obtained for the green rust samples analyzed in this work. The EDX

spectra show that the areas of each sample imaged contain gold. The large copper peaks in Figures 11, 12, 13, and 14 are due to the copper grids on to which the samples were loaded. The morphology of the iron phases in the TEM images of the green rust samples are obviously different from the morphology observed in the SEM images of the same samples (Figs. 6 and 7). The images obtained by SEM show the green rust as an amorphous precipitate whereas the TEM images show well formed acicular crystals a few hundreds of angstroms wide and a few thousands of angstroms long.

The formation of these crystals was directly observed during sample preparation for TEM analysis as a transformation of the blue green green rust phase to an orange brown phase upon suspension of the sample in water. Since green rust is an intermediate phase in the oxidation of Fe^{2+} (aq) to Fe^{3+} (oxy)hydroxides and the crystals are acicular it seems very
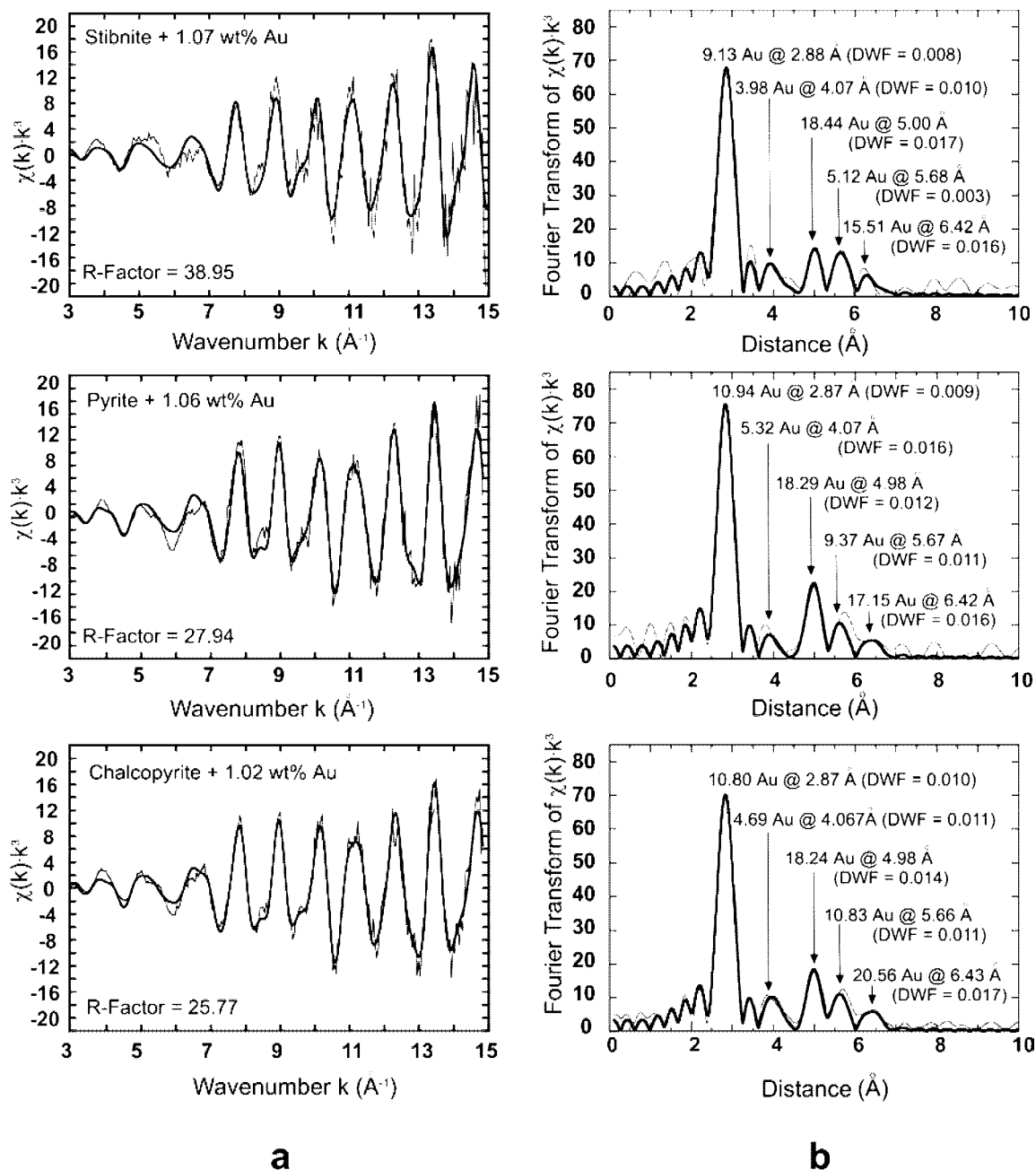
FIGURE 5. (**a**) k^3 weighted EXAFS spectra for gold after reaction of aqueous Au^{3+} with sulfide minerals. (**b**) Fourier transforms of the k^3 weighted EXAFS spectra.

likely that this phase is goethite. This was confirmed by XRD analysis of an aliquot of the green rust with 0.1 wt% gold sample used for TEM analysis. The difference is due to the fact that the green rust samples prepared for SEM analysis were mounted and loaded directly into the SEM whereas the samples prepared for TEM analysis had to be suspended in water before mounting and loading into the TEM and this step was sufficient to oxidize the green rust to goethite.

The TEM images of the green rust samples show that there are no obvious features that could be interpreted as metallic gold clusters. This could be because there is not sufficient difference in contrast between the goethite and the gold clusters or that they are too small to be resolved by the TEM (<5 nm or <50 Å). A TEM study of gold associated with goethite shows that metallic gold clusters are formed after hydrolysis of a ferrihydrite suspension containing Au^{3+} (Greffie et al. 1996). The individual gold clusters are clearly seen in the TEM images as very dark sub circular features of 30 to 600 Å in diam-
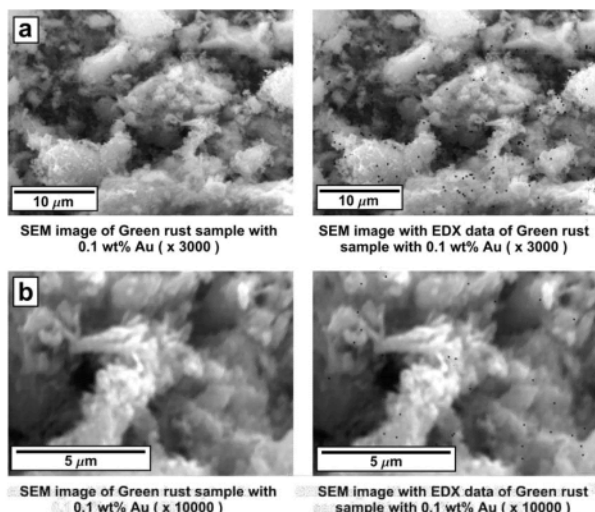
FIGURE 6. SEM and EDX images of green rust +0.1 wt% gold.
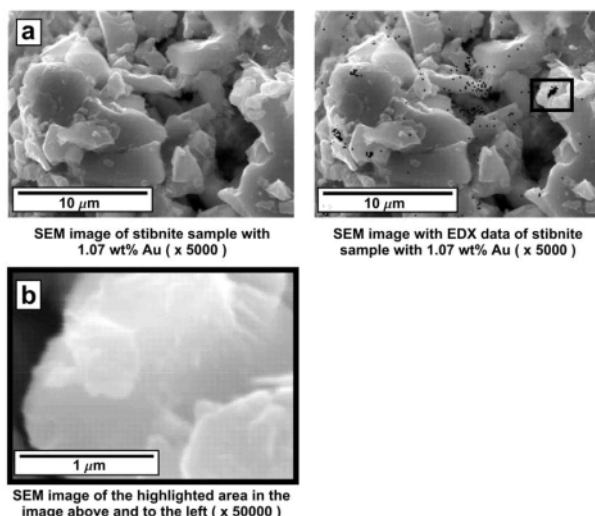
FIGURE 8. SEM and EDX images of stibnite +1.07 wt% gold.
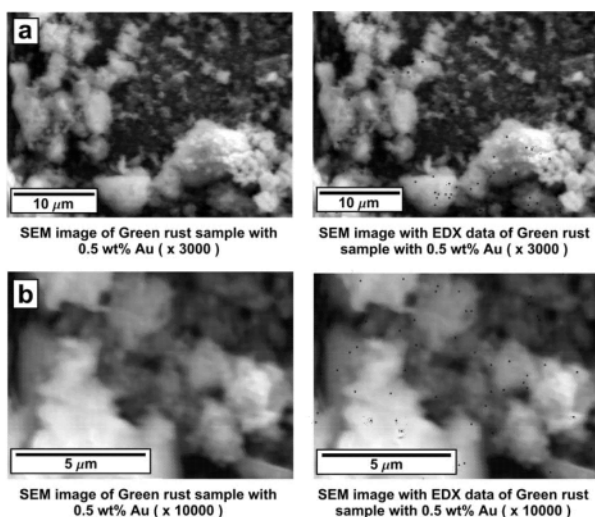
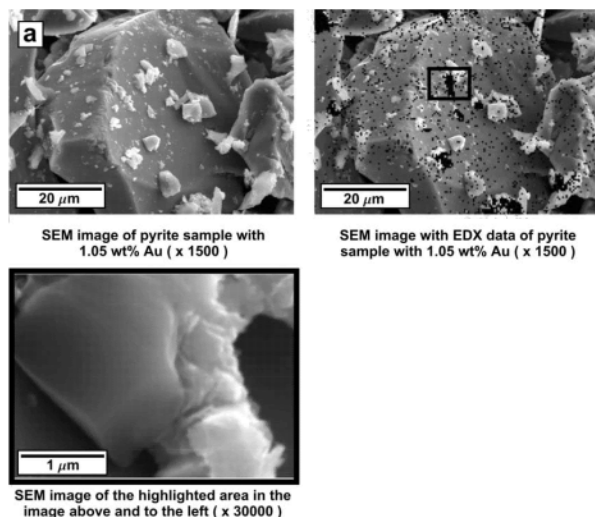**FIGURE 7.** SEM and EDX images of green rust +0.5 wt% gold.

FIGURE 9. SEM and EDX images of pyrite +1.05 wt% gold.

eter or composite clusters representing multiple twinned particles up to 1500 Å in diameter growing on the edges of the goethite lathes. This suggests that if the metallic gold clusters present in the oxidized green rust samples are large enough to be resolved by TEM then they would be clearly visible, therefore the gold clusters in this study are <50 Å in diameter. This size is in good agreement with the size calculated for the green rust sample with 0.5 wt% gold (28.64–36 Å).

The TEM images and EDX spectra of the stibnite samples are shown in Figure 12. The TEM images show that there are no features that could be interpreted as individual metallic gold clusters. TEM images of natural samples of "invisible" gold found in association with stibnite show that gold is clearly seen as dark black spheres (400–1000 Å in diameter) located in microfissures and in grain interstices of the lighter stibnite particles (Yang et al. 1998). The TEM images (Fig. 12) do contain some darker areas of similar size to those observed in the natural samples (100–320 Å) associated with the finer mineral grains
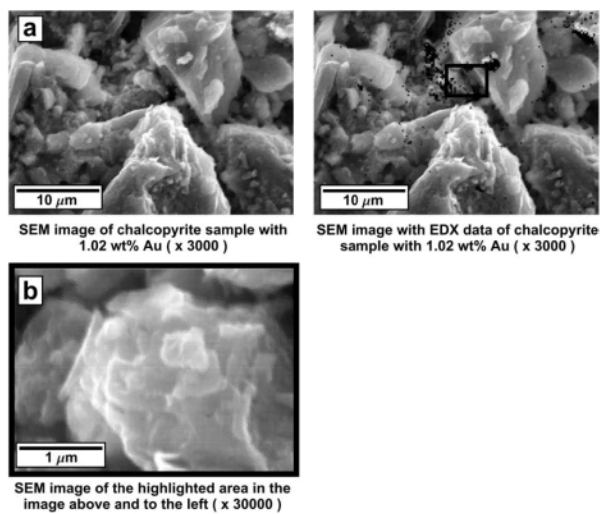

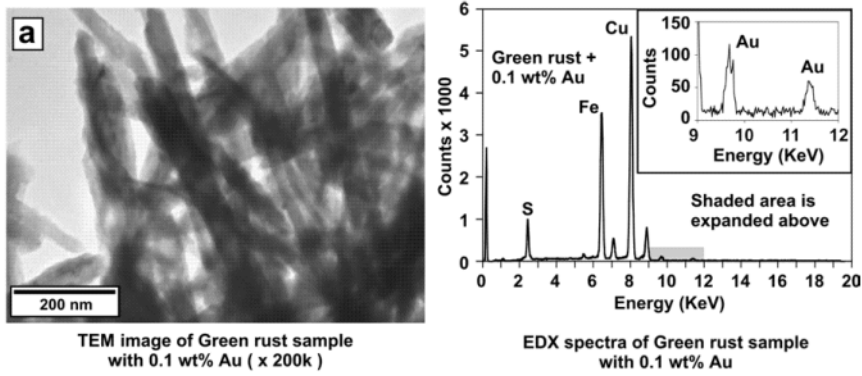**FIGURE 10.** SEM and EDX images of chalcopyrite +1.02 wt% gold.

FIGURE 11. TEM images and EDX spectra of the green rust samples with (**a**) 0.1 wt% gold and (**b**) 0.5 wt% gold.
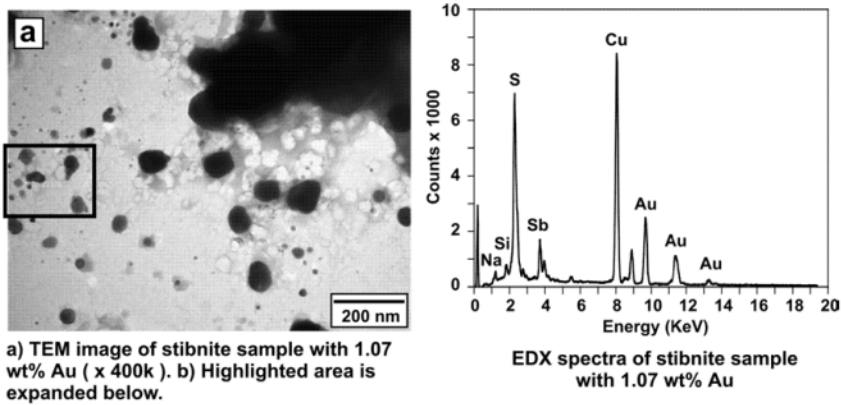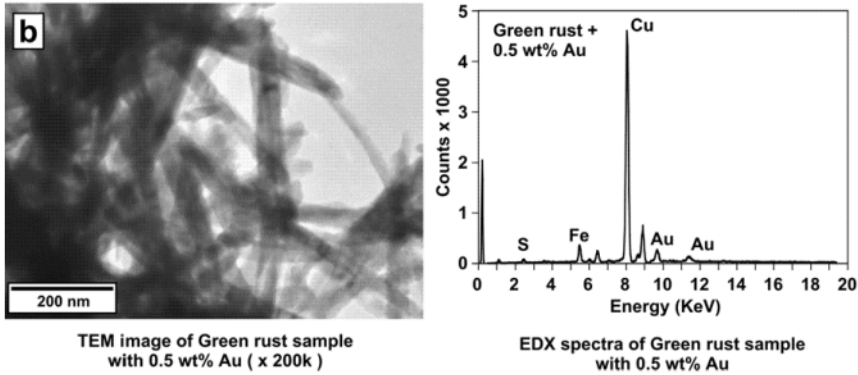
TEM image of Green rust sample with 0.1 wt% Au (x 200k)

EDX spectra of Green rust sample with 0.1 wt% Au

TEM image of Green rust sample with 0.5 wt% Au (x 200k)
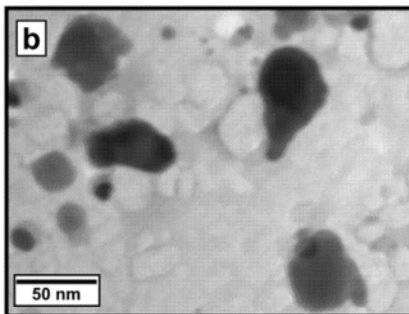
EDX spectra of Green rust sample with 0.5 wt% Au

FIGURE 12. (**a**) TEM images and EDX spectrum of the stibnite sample with 1.07 wt% gold. (**b**) Expanded image of the highlighted area in **a**.
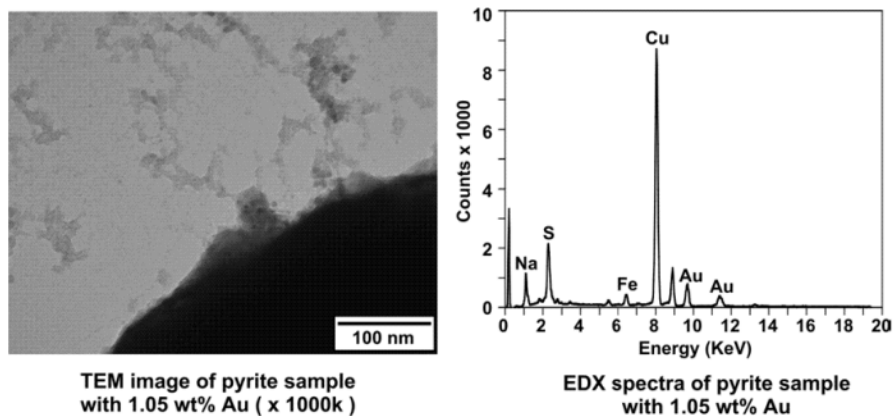
a) TEM image of stibnite sample with 1.07 wt% Au (x 400k). b) Highlighted area is expanded below.

EDX spectra of stibnite sample with 1.07 wt% Au

TEM image of pyrite sample
with 1.05 wt% Au (x 1000k)

EDX spectra of pyrite sample
with 1.05 wt% Au

FIGURE 13. TEM image and EDX spectrum of the pyrite sample with 1.06 wt% gold.

a) TEM image of chalcopyrite sample with
1.02 wt% Au (x 400k). b) Highlighted area is
expanded below.

EDX spectra of chalcopyrite sample
with 1.02 wt% Au
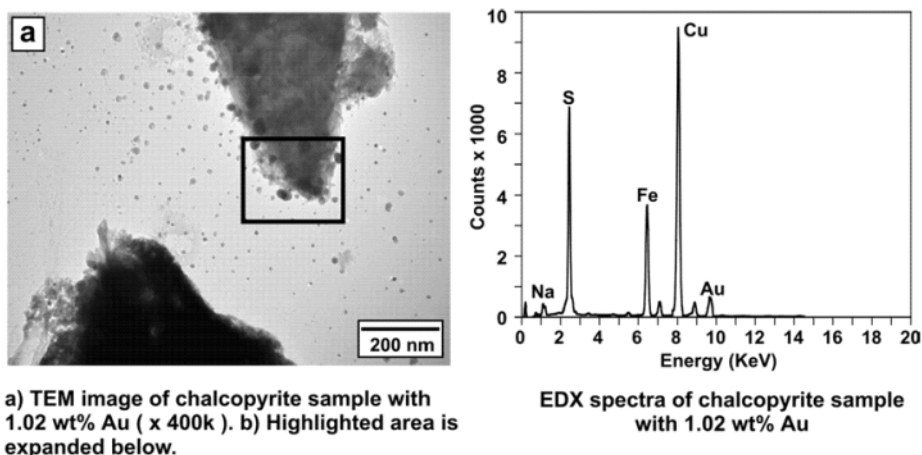
FIGURE 14. (**a**) TEM images and EDX spectrum of the chalcopyrite sample with 1.02 wt% gold. (**b**) Expanded image of the highlighted area in **a**.

(Fig. 12b) but we do not think that these features correspond to individual metallic gold clusters. On closer examination some of these darker features appear to be where mineral grains overlap, as none are as clearly defined as those observed in the study of Yang et al. (1998) and they do not appear to form the particles of regular spherical morphology (Yang et al. 1998) exhibited by metallic gold. Another possibility is that these features in Figure 12b are irregular aggregates of smaller gold clusters (Maddox et al. 1994). The diameter of any individual metallic gold cluster in this sample is therefore thought to be below the resolution of the TEM used in this work (<5 nm or <50 Å) though considering the EXAFS data and the study of

Maddox et al. (1994) it is possible that they are forming composite clusters a few hundreds of angstroms in diameter.

Figure 13 shows a TEM image and the EDX spectra of the sample of pyrite containing 1.05 wt% gold. The EDX spectra clearly shows that gold is present in this sample and the EXAFS show that this gold is present as metallic gold; however, the image contains no features that may be interpreted as metallic gold clusters. TEM images of natural samples of "invisible" gold found in association with pyrite show that gold is clearly seen as dark black spheres (1000–2000 Å in diameter) either seen individually or forming chains on growth surfaces of the much lighter pyrite mineral grains (Yang et al. 1998). In con-

trast to this, the pyrite grain shown in Figure 13 is very dark and this may mean that the clusters may be present but there is an insufficient difference in contrast between the pyrite and the gold for the clusters to be visible. This means that it is very difficult, based on the TEM analysis, to apply any constraints on the size of the metallic gold clusters present in this sample. Again the possibility that the any individual gold clusters are forming composite clusters should be considered and if they are present they have a maximum size of 5000 Å since they are not resolved in the SEM images (Fig. 9).

The darker features present in the TEM images of the chalcopyrite sample with 1.02 wt% gold (Fig. 14a) may represent metallic gold clusters 100 to 440 Å in diameter but on closer inspection (Fig. 14b) some resemble the darker areas of the stibnite sample in that some of them are caused by overlapping mineral grains and none represent the typical gold morphologies seen in TEM studies of gold reduction by minerals. As with the stibnite sample it is also possible that these dark irregular features are composite clusters of smaller gold clusters. It is thought that, like the stibnite sample, any individual clusters present in this sample are too small to be resolved by the TEM and therefore must have a maximum diameter of 50 Å.

Assignment of average sizes to metallic gold clusters

The EXAFS data for the green rust sample with 0.1 wt% gold suggests a metallic gold particle size of between 32 and 241 Å, however no gold particles are visible on the TEM images; therefore the upper limit of this range can be constrained to 50 Å. The XANES and EXAFS data suggest that these clusters probably have five shells and are therefore at least 36 Å in diameter. The size range of the particles present in this sample is therefore between 36 and 50 Å. The TEM images of the green rust with 0.5 wt% gold also constrain the maximum size of the metallic gold clusters present in this sample to 50 Å. The good quality of fit of the EXAFS data strongly suggest that the clusters may be slightly smaller than this, with diameters between 29 and 36 Å.

The diameter of any individual gold clusters present in the stibnite sample suggested by the TEM work is in good agreement with the cluster sizes implied by the EXAFS and XANES data (at least 36 Å). Although the EXAFS data gives a cluster size of 19 to 77 Å, the TEM work constrains the size to below 50 Å. This is in good agreement with the minimum size suggested by the normalized XANES data (five to six shells, 36 to 42.96 Å) but this conclusion should be considered wholly qualitative. The value for N_1 for this sample is 9.13 (diameter is 30 Å), which seems a slight underestimation of the immediate coordination environment because the sample contains five shells (equivalent to N_1 of 9.63), four of which have co-ordinations in good agreement with the predicted values. Therefore the diameter of any individual metallic gold clusters and those which may be forming composite clusters in this sample is between 36 and 50 Å.

The dark appearance of pyrite in the TEM means that this data cannot be used to constrain the size of the individual gold clusters present in this sample. The EXAFS data suggests a size range of 27 Å to at least 77 Å but the high value of N_1 (10.94) means that +20% error in N_1 gives a value for N_1 for

which Equation 7 is not valid (i.e., >12) and therefore these data cannot be used to unambiguously constrain the upper size limit of the individual clusters present in this sample. The XANES spectrum of this sample and the good agreement in predicted and measured co-ordination numbers for all five shells suggests that there are at least five co-ordination shells, corresponding to a minimum size of 36 Å. A best estimate of the maximum size of the individual particles of 77 Å could be made on the basis that the good fit of the theoretical model to the EXAFS data (R-factor is 27.94) implies reliability in the value of N_1, however, this should be considered tentative at best.

The EXAFS data from the chalcopyrite sample with 1.02 wt% gold implies that the individual metallic gold clusters present in this sample are between 26 Å and at least 68 Å and the upper size limit of individual clusters is further constrained by the TEM images to 50 Å. The good agreement between theoretical model and the EXAFS data (R-factor is 25.77) and the theoretical co-ordination numbers and experimentally measured values for all five shells is strong evidence that there are at least five shells present. The average size range for the individual metallic gold clusters in this sample is therefore 36 to 50 Å and they may be forming composite clusters a few hundreds of angstroms in diameter.

The average size ranges for the clusters present in all of the samples analyzed are summarized in Table 8.

Comparisons with previous studies

In studies of gold reduction in laterites, Mann (1983, 1984) proposed ferrolysis as the mechanism of metallic gold accumulation in these types of deposits. The last stage of ferrolysis, the precipitation of metallic gold with oxidized iron minerals, was studied by Greffie et al. (1996) by co-precipitating metallic gold with goethite and ferrihydrite. They observed individual particles of "invisible" gold between 30 and 600 Å and composite clusters consisting of multiple twinned particles up to 1500 Å in diameter. The work presented here has shown that the overall process of ferrolysis is likely to be more complex in that aqueous Au^{3+} will not only be reduced by aqueous Fe^{2+} to form metallic gold but will also be reduced by Fe^{2+} present in partially oxidized intermediate iron phases to produce the submicroscopic "invisible" gold.

The individual clusters produced in the green rust samples are smaller than those produced by the work of Greffie et al. (1996) and no composite clusters are observed. The difference between this work and the study of Greffie et al. (1996) probably lies in the methods that were used to reduce the Au^{3+} and the minerals that were used in the experiments. This suggests that the oxidation potential and mineral phases present in the system may influence the size and morphology of the gold par-

TABLE 8. Summary of approximate average sizes for the gold clusters formed in all the samples analyzed

Sample	Min. size Å	Max. size Å	Composite cluster size
Green Rust + 0.1 wt% Au	36	50	
Green Rust + 0.5 wt% Au	29	36	
stibnite + 1.07 wt% Au	36	50	≤320 Å
pyrite + 1.05 wt% Au	36	77	≤5000 Å
chalcopyrite + 1.02 wt% Au	36	50	≤440 Å

ticles found in nature. The gold particles produced in this work and that of Greffie et al. (1996) are much smaller than those observed in nature. For example some of the "invisible" gold found associated with iron oxide minerals at the Kori Kollo deposit (Bolivia) forms irregular shaped particles approximately 1000 Å in size (Darke et al. 1997). A study of the physicochemical and experimental conditions that produce different sizes and morphologies of gold particles during ferrolysis may yield information relating to the conditions under which lateritic "invisible" gold forms in nature. Another factor that may influence the mechanism of "invisible" gold formation is the concentration of gold in solution. Due to technical constraints it is necessary to use gold concentrations at least five to six orders of magnitude higher than those found in nature. This may lead to the formation of smaller clusters since at higher concentrations the nucleation rate will be higher.

Previous SEM studies of the reaction of gold with sulfide minerals demonstrated that almost instantaneous reduction at the mineral surface does occur. The sizes of the gold clusters produced in those experiments range from approximately 2000 Å (Mycroft et al. 1995) to tens of microns (Scaini et al. 1997).

In addition to this the formation of composite clusters of smaller gold clusters was observed on the surface of arsenopyrite (200–500 Å) and pyrite (3800 Å). The individual metallic gold clusters produced by the experiments presented here are between 36 and 77 Å in diameter and probably form composite clusters of a few hundreds of angstroms in diameter on the surface of stibnite and chalcopyrite and up to 5000 Å on the surface of pyrite.

Yang et al. (1998), using TEM, observed "invisible" gold particles with an average size of 1500 Å in natural samples of pyrite and stibnite but due to the relatively low magnification of these images (×10 000 to ×28 000) it is not possible to determine whether these particles are individual or composite metallic gold clusters. If they are composite clusters then they are of a similar size to those synthesized by Maddox et al. (1994) [gold (aq) is 10^{-5} to 10^{-4} M] and some of the features observed in this work [gold (aq) is 10^{-3} M]. This suggests that the concentration of gold does not affect particle size when sulfide minerals reduce aqueous gold. This is confirmed by the study of Maddox et al. (1994), which shows that the rate of deposition, and therefore the size of the gold clusters, is dependant on the oxidation rate of the mineral.

The major problem with this and previous experimental studies of "invisible" gold formation is that they are performed under ambient laboratory conditions and therefore more elaborate experiments, mimicking the physico-chemical conditions found in hydrothermal deposits, are needed to provide a better understanding of the conditions under which "invisible" gold forms in these systems.

REFERENCES CITED

Ashley, P.M., Creagh, C.J., and Ryan, C.G. (2000) Invisible gold in ore and mineral concentrates from the Hillgrove gold-antimony deposits, NSW, Australia. Mineralium Deposita, 35, 285–301.
Atkins, P.W. (1994) Physical Chemistry, 5th ed. Oxford University Press, U.K.
Baes, C.F. and Mesmer, R.E., Eds. (1976) Hydrolysis of Cations, 1st ed. Wiley, New York.
Baranova, N.N. and Ryzhenko, B.N. (1981) Computer simulation of the Au-Cl-S-Na-H₂O system in relation to the transport and deposition of gold in hydrothermal processes. Geokhimiyia, 7, 989–1001.
Bender Koch, C. and Mörup, S. (1991) Identification of green rust in an ochre sludge. Clay Mineralogy, 26, 577–582.
Benfield, R.E. (1992) Mean co-ordination numbers for Non-metal-Metal transition in clusters. Journal of the Chemical Society, Faraday Transactions, 88, 1107–1110.
Benfield, R.E., Grandjean, D., Kröll, M., Pugin, R., Sawitowski, T., and Schmid, G. (2001) Structure and bonding of gold metal clusters, colloids and nanowires studied by EXAFS, XANES and WAXS. Journal of Physical Chemistry B, 105, 1961–1970.
Benning, L.G. and Seward, T.M. (1996) Hydrosulphide complexing of Au (I) in hydrothermal solutions from 150–400 °C and 500–1500 bar. Geochimica et Cosmochimica Acta, 60, 1849–1871.
Berzon, R.O., Bryzgalov, I.A., Konyshev, V.O., Meshcherina, T.V., and Nekrasova, A.N. (1999) Geological setting, mineral composition and formation conditions of the Kyuchus gold-mercury deposit Sakha, Russia. Geology of Ore Deposits, 41, 440–459.
Bethke, C.M., Ed. (1994) The Geochemists Workbench, v2.0: A users guide to Rxn, Act2, Tact, React and Gtplot. University of Illinois, Champaign-Urbana.
Binstead, N., Campbell, J.W., Gurman, S.J., and Stephenson, P.C. (1998) SERC Daresbury Laboratory EXCURV98 program, Daresbury, U.K.
Bowell, R.J., Baumann, M., Gingrich, M., Tretbar, D., Perkins, W.F., and Fisher, P.C. (1999) The occurrence of gold at the Getchell mine, Nevada. Journal of Geochemical Exploration, 67, 127–143.
Cardille, C.M., Cashion, J.D., McGrath, A.C., Renders, P., and Seward, T.M. (1993) ¹⁹⁷Au Mössbauer study of Au₂S and gold adsorbed onto As₂S₃ and Sb₂S₃ substrates. Geochimica et Cosmochimica Acta, 57, 2481–2486.
Cloke, P.L. and Kelly, W.C. (1964) Solubility of gold under inorganic supergene conditions. Economic Geology, 59, 259–270.
Cook, N.J. and Chryssoulis, S.L. (1990) Concentrations of invisible gold in the common sulphides. Canadian Mineralogist, 28, 1–16.
Darke, K.E., Boyce, A.J., Clapperton, C.M., Fallick, A.E., Redwood, S.D., and Rice, C.M. (1997) Supergene mineralisation at the Kori Kollo gold Mine, Bolivia. Exploration and Mining Geology, 6, 209–221.
Dent, A.J. and Mosselmans, J.F.W. (1992) A Guide to EXBACK, EXCALIB and EXCURVE92. CLRC Daresbury Laboratory internal document, Daresbury, U.K.
Enzweiler, J. and Joekes, I. (1991) Adsorption of colloidal gold on colloidal iron oxides. Journal of Geochemical Exploration, 40, 133–142.
Farges, F., Sharps, J.A., and Brown, G.E. (1993) Local environment around gold (III) in aqueous chloride solutions: An EXAFS spectroscopy study. Geochimica et Cosmochimica Acta, 57, 1243–1252.
Fleet, M.E. and Mumin, A.H. (1997) Gold-bearing arsenian pyrite and marcasite and arsenopyrite from Carlin Trend gold deposits and laboratory synthesis. American Mineralogist, 82, 182–193.
Fleming, C.A. (1992) Hydrometallurgy of precious metals recovery. Hydrometallutgy, 30, 127–162.
Fletcher, D.A., McMeeken, R.F., and Parkin, D.J. (1996) The United Kingdom Chemical Database Service. Journal of Chemical and Information Computing Science, 36, 746–749.
Foster, R.P., Ed. (1984) Gold '82, 1st ed. Balkema, Neatherlands.
Fritsche, H.G. and Benfield, R.E. (1993) Exact analytical formulae for mean co-ordination numbers in clusters. Atoms and Molecular Clusters, 26, 15–17.
Greffie, C., Benedetti, M., Parron, C., and Amouric, M. (1996) Gold and iron oxide associations under supergene conditions: An experimental approach. Geochimica et Cosmochimica Acta, 60, 1531–1542.
Gurman, S.J. (1988) The small atom approximation theory. Journal of Physics C: Solid State Physics, 21, 3699–3717.
Gurman, S.J., Binstead, N., and Ross, I. (1984) Single scattering curved wave theory. Journal of Physics C: Solid State Physics, 17, 143–151.
Hannington, M.D., Tivey, M.K., Larocque, A.C.L., Petersen, S., and Rona, P.A.

(1991) The occurrence of gold in sulphide deposits of the TAG Hydrothermal Field, Mid-Atlantic Ridge. Canadian Mineralogist, 33, 1285–1310.

Hedin, L. and Lundqvist, S. (1969) Effects of electron-electron and electron-phonon interactions on the one-electron states of solids. Solid State Physics, 23, 1–181.

Henley, R.W. (1973) Solubility of gold in hydrothermal chloride solutions. Chemical Geology, 11, 73–87.

Hong, H.L., Wang, Q.Y., Chang, J.P., Liu, S.R., and Hu, R.Z. (1999) Occurrence and distribution of invisible gold in the Shewushan supergene gold deposit, southeastern Hubei, China. Canadian Mineralogist, 37, 1525–1531.

Hyland, M.M. and Bancroft, G.M. (1989) An XPS study of gold deposition at low temperatures on sulphide minerals: Reducing agents. Geochimica et Cosmochimica Acta, 53, 367–372.

Jean, G.E. and Bancroft, G.M. (1985) An XPS and SEM study of gold deposition at low temperatures on sulphide mineral surfaces: Concentration of gold by adsorption/reduction. Geochimica et Cosmochimica Acta, 49, 979–987.

Karasyova, O.N., Ivanona, L.I., Lakshtanov, L.Z., Lövgren, L., and Sjöberg, S. (1998) Complexation of gold(III)-chloride at the surface of hematite. Aquatic Geochemistry, 4, 215–231.

Krauskopf, K.B. (1951) The solubility of gold. Economic Geology, 46, 61–84.

Machesky, M.L., Andrade, W.O., and Rose, A. (1991) Adsorption of gold (III)-chloride and gold (I)-thiosulphate anions by goethite. Geochimica et Cosmochimica Acta, 55, 769–776.

Maddox, L.M., Bancroft, G.M., Scaini, M.J., and Lorimer, J.W. (1994) Invisible gold: Comparison of Au deposition on pyrite and arsenopyrite. American Mineralogist, 83, 1240–1245.

Mann, A.W. (1983) Hydrogeochemistry and weathering of the Yilgarn Block, Western Australia—ferrolysis and heavy metals in continental brines. Geochimica et Cosmochimica Acta, 47, 181–190.

——— (1984) Mobility of gold and silver in lateritic weathering profiles: Some observations from Western Australia. Economic Geology, 79, 38–49.

Mao, S.H. (1991) Occurrence and distribution of invisible gold in a Carlin-type gold deposit in China. American Mineralogist, 76, 1964–1972.

Matel, N.L., Kolpakova, N.N., and Il'ina, G.F. (2000) Genetic features of the Darasun gold-sulphide deposit (Eastern Transbaikal Region). Geology of Ore Deposits, 42, 474–495.

McHugh, J.B. (1988) Concentration of gold in natural waters. Journal of Geochemical Exploration, 30, 85–94.

Mehrabi, B., Yardley, B.W.D., and Cann, J.R. (1999) Sediment-hosted disseminated gold mineralisation at Zarshuran. Mineralium Deposita, 34, 673–696.

Mernagh, T.P., Heinrich, C.A., Leckie, J.P., Carville, D.P., Gilbert, D.J., Valenta, R.K., and Wyborn, L.A.I. (1994) Chemistry of low temperature hydrothermal gold, platinum and palladium (± uranium) mineralisation at Coronation Hill, Northern-Territory, Australia. Economic Geology, 89, 1053–1073.

Michibayashi, K. (1995) Two phase syntectonic gold mineralisation and barite remobilisation within the main ore body of the Golden Giant Mine, Hemlo, Ontario, Canada. Ore Geology Reviews, 10, 31–50.

Muller, D., Franz, L., Herzig, P.M., and Hunt, S. (2001) Potassic igneous rocks from the vacinity of epithermal gold mineralisation, Lihir Island, Papua New Guinea. Lithos, 57, 163–186.

Murphy, J.A. and LaGrange, M.S. (1998) Raman spectroscopy of gold chloro-hydroxy speciation in fluids at ambient temperature and pressure: A re-evaluation of the effects of pH and chloride concentration. Geochimica et Cosmochimica Acta, 62, 3515–3526.

Murphy, J.A., Stevens, G., and LaGrange, M.S. (2000) The effects of temperature and pressure on gold-chloride speciation in hydrothermal fluids: A Raman spectroscopic study. Geochimica et Cosmochimica Acta, 64, 479–494.

Mycroft, J.R., Bancroft, G.M., McIntyre, N.S., and Lorimer, J.W. (1995) Spontaneous deposition of gold on pyrite from solutions containing Au (III) and Au (I)

chlorides, Part 1, A surface study. Geochimica et Cosmochimica Acta, 59, 3351–3365.

Nechayev, Y.A. (1984) The effects of solution composition on the adsorption of gold (III) complexes on hematite. Geokhimiyia, 4, 527–533.

Oberthur, T., Weiser, T., Amanor, J.A., and Chryssoulis, S.L. (1997) Mineralogical siting and distribution of gold in quartz veins and sulphide ores of the Ashanti mine and other deposits in the Ashanti belt of Ghana: Genetic implications. Mineralium Deposita, 32, 2–15.

Peck, J.A., Tait, C.D., Swanson, B.I., and Brown, G.E. (1991) Speciation of aqueous gold (III) chlorides from ultraviolet/visible absorption and RAMAN/resonance RAMAN spectroscopies. Geochimica et Cosmochimica Acta, 55, 671–676.

Renders, P.J. and Seward, T.M. (1989) The adsorption of thio gold(I) complexes by amorphous As$_2$S$_3$ and Sb$_2$S$_3$ at 25 °C and 90 °C. Geochimica et Cosmochimica Acta, 53, 255–267.

Rubin, J.N. and Kyle, J.R. (1997) Precious metal mineralogy in porphyry, skarn, and replacement-type ore deposits of the Ertsberg (Gunung Bijih) district; Irian Jaya, Indonesia. Economic Geology, 92, 535–550.

Santaguida, F. and Hannington, M.D. (1996) Characteristics of gold mineralisation in volcanogenic massive sulphide deposits of the Notre Dame Bay Area, central Newfoundland. Canadian Journal of Earth Sciences, 33, 316–334.

Scaini, M.J., Bancroft, G.M., and Knipe, S.W. (1997) An XPS, AES and SEM study of gold and silver chloride species with PbS and FeS$_2$: Comparison to natural samples. Geochimica et Cosmochimica Acta, 61, 1223–1231.

Schoonen, M.A.A., Fisher, N.S., and Wente, M. (1992) Gold sorption onto pyrite and goethite: A radiotracer study. Geochimica et Cosmochimica Acta, 56, 1801–1814.

Schwertmann, U. and Fetcher, H. (1994) The formation of green rust and its transformation to lepidocrocite. Clay Mineralogy, 29, 87–92.

Seward, T.M. (1973) Thio complexes of gold and the transport of gold in hydrothermal ore solutions. Geochimica et Cosmochimica Acta, 37, 379–399.

——— (1984) The transport and deposition of gold in hydrothermal systems. In R.P. Foster, Ed., Gold 82, 1st ed., 165–181. Balkema, Neatherlands.

Shenberger, D.M. and Barnes, H.L. (1989) Solubility of gold in aqueous sulphide solutions from 150 to 350 °C. Geochimica et Cosmochimica Acta, 53, 269–278.

Spry, P.G. and Thieben, S.E. (2000) The distribution and recovery of gold in the Golden Sunlight gold-silver telluride deposit, Montana, USA. Mineralogical Magazine, 64, 31–42.

Stumm, W. and Morgan, J.J., Eds. (1981) Aquatic Chemistry, 1st ed. Wiley, New York.

Valeton, I. (1994) Element concentration and formation of ore deposits by weathering. Catena, 21, 99–129.

Vlassopoulos, D. and Wood, S.A. (1990a) Gold speciation in natural waters: I. Solubility and hydrolysis reactions of gold in aqueous solution. Geochimica et Cosmochimica Acta, 54, 3–12.

——— (1990b) Correction. Geochima et Cosmochima Acta, 54, 1849.

Watkins, J.W., Elder, R.C., Greene, B., and Darnell, D.W. (1987) Determination of gold binding in algal biomass using EXAFS and XANES spectroscopies. Inorganic Chemistry, 26, 1147–1151.

Yang, S., Blum, N., Rahders, E., and Zhang, Z. (1998) The nature of invisible gold in sulphides from the Xiangxi Au-Sb-W ore deposit in Northwestern Hunan, Peoples Republic of China. Canadian Mineralogist, 36, 1361–1372.